SplitFlyer Air: A Modular Quadcopter that Disassembles into Two Bicopters Mid-Air

Songnan Bai and Pakpong Chirarattananon

***Abstract*—Motivated by the flight ability of severely underactuated rotorcraft, we introduce a transformable quadcopter—SplitFlyer Air. The novel vehicle consists of two bicopter modules, each equipped with only two propellers and capable of position-controlled flight. Despite the notable difference in their flight regimes, the robots, in both bicopter and quadcopter configurations, can be modeled and controlled by a single framework. In the flight experiments, an undocking mechanism with preloaded elastic energy was designed and employed to assist the SplitFlyer Air to disassemble autonomously. The catapult-inspired mechanism provides initial yaw rates for the bicopters, accelerating them to reach their hovering states without losing stability or substantial altitude. Thanks to the developed controller and devised mechanism, the transformation flights can be reliably achieved. The ability to disassemble mid-air shows promise for search and rescue missions or other swarm applications as it allows the flock size to adaptively grow on demand.**

I. Introduction

THE rapid advancement of micro aerial vehicles (MAVs) has brought along a plethora of potential applications in several domains, such as agriculture, inspection, and reconnaissance [1]. Thanks to the recent progress in platform developments and navigation, aerial robots are expected to demonstrate even more functionalities in order to accomplish increasingly complex tasks. Such efforts, for instance, have been manifested by the realization of multi-modal locomotion [2]–[4], robotic swarms [5]–[7], autonomous navigation [8], [9], and modular or reconfigurable vehicles [10]–[13].

Previously developed multirotor MAVs with modular reconfigurability can be classified according to the flight capability of their base modules. Equipped with four propellers, each unit of ModQuads [10], [14] is capable of flying independently. This allows the robots to demonstrate mid-air assembly [10] or disassembly [14] depending on the mechanism fitted on the airframe. On the other hand, each base module of the DFA [15], DRAGON [16], or UFOs [12] is comprised of either one or two propellers, rendering it incapable of flight by itself.

Nevertheless, there exist several severely underactuated flying robots that achieve 3D position control despite possessing only one or two actuators. Samara-type vehicles with two actuators fly by rotating around the vertical axis during flight [17], [18]. Flapping-wing robots with two bimorph piezoelectric actuators [19] or motors [20] demonstrate outstanding flight agility by leveraging sinusoidal driving signals. A similar feat has been accomplished with severely underactuated multirotor MAVs [21], mostly as a flight strategy for quadcopters suffering from rotor failures through the use of cyclic commands [22]–[24]. From the perspective of flight dynamics and modular robotics, this implies that a conventional quadcopter can be regarded as a collection of multiple flight-capable base modules.

This work was supported by the Research Grants Council of the Hong Kong Special Administrative Region of China (grant numbers CityU-11215220)

The authors are with the Department of Biomedical Engineering, City University of Hong Kong, Hong Kong SAR, China (email: pakpong.c@cityu.edu.hk).

To this end, we report the development of SplitFlyer Air, a quadcopter that can transform into two self-contained bicopters mid-air, each with the ability to fly independently despite having only two propellers. To do so, SplitFlyer Air is constructed by fastening two bicopters with power and control autonomy. Compared with our preliminary prototype [25], Splitflyer Air is equipped with an undocking mechanism to permit two flight units to safely and autonomously separate mid-air as demonstrated in the supplementary video. The added ability is brought by the increased vehicle size and its associated improved payload capacity. It is foreseeable that when deployed as a group, SplitFlyers Air has the ability to increase the flock size according to the changing mission requirement, raising their potential in search and rescue operations or other swarm applications. Starting as quadcopters, the small group size eases the control and collision avoidance tasks. The robots then break into subunits when they are required to follow multiple targets or explore different paths. In addition, compared with a regular multirotor vehicle [26]–[28], the revolving bicopter may benefit from a wider vision. The fast self-rotation flight allows a camera or a laser ranging sensor with a limited field of view to scan the surroundings at different phases of rotation. A high bandwidth sensor can be employed to yield a 360° detection as found in [29]–[31].

To stabilize the attitude and control the position of bicopters, the challenge lies in the severe underactuation of the platform. With two propellers of the same spinning direction, each bicopter revolves around its vertical axis in flight and the magnitude of the total thrust is tightly coupled with the vehicle's non-zero yaw rate. Thus far, the modeling and control of such vehicles have been accomplished based on the notion of relaxed attitude control [21], [23], or, similarly, primary-axis attitude control [24]. Such strategies center on manipulation of the primary rotational axis of the vehicle, defined as the cycle-averaged thrust direction as seen in the inertial frame. Then, flight control is generally achieved by the application of linear system techniques through linearization [21], [22] or cascade control near the hovering solutions [23], [24]. In [23], [24], for example, position control is attained in the outer loop by directing the primary rotation axis towards the desired direction. Then, the inner loop control is responsible

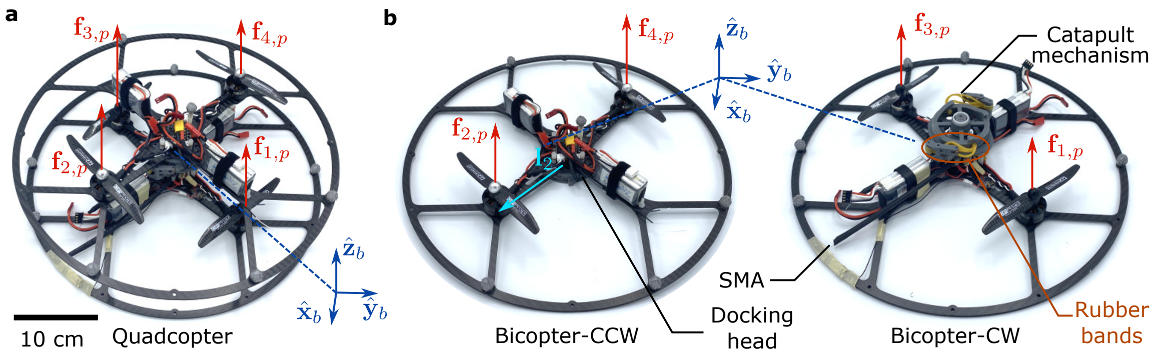

Fig. 1. Photographs of SplitFlyer Air. (a) The quadcopter is comprised of two flight-capable bicopter subunits, distinguished by the spinning direction of the propellers: Bicopter-CCW and Bicopter-CW. (b) Bicopter-CCW, with a pair of counterclockwise propellers, is equipped with a docking head (underneath, not visible). (c) Bicopter-CW, with a pair of counterclockwise propellers, carries the catapult mechanism on top. An entire robot is constructed from two bicopters docked together.

for aligning the body axis with the desired direction.

Despite the notable difference in flight condition, both quadcopters and bicopters can be modeled by the same set of equations, which also allows the use of a single set of the control framework for both platforms. To achieve this, we employ the concept of reduced attitude dynamics [21], [23], [24] and regard the quadcopter or the bicopter as an axisymmetric rigid disc with an approximately constant revolving speed. When the equations of motion are derived in the inertial frame, the translational and attitude dynamics are inherently and tightly coupled, whether they are for quadcopters or bicopters. As a result, position and attitude control is achieved simultaneously without the use of cascaded control loops as previously seen in rotating rotorcraft [21]–[24]. The elimination of the cascaded structure renders the proposed controller resembles high-performance nonlinear controllers developed for conventional MAVs [7], [12], [19], [28]. To do so, the condition of small deviations from the hovering state is assumed, similar to previous works [21]–[24]. Furthermore, the proposed method leverages the symmetrical design of the bicopters. The development, particularly the compatibility with a quadcopter and the removal of the cascaded structure, is also a significant expansion from our preliminary result [25]. The changes result in markedly enhanced flight performance.

In addition to the novel approach on flight control of severely underactuated multirotor robots, we demonstrate the autonomous in-flight transition of SplitFlyer Air from the quadcopter mode to bicopters. This is an ability absent from the early prototypes in [25] and also distinct from existing modular MAVs [10], [12], [14]–[16]. The difficulty in accomplishing the task stems from the vastly different hovering conditions of both platforms. While a quadcopter is capable of steady hovering, a bicopter needs to swiftly reach its nominal revolving rate to stay aloft. As a consequence, immediately after dividing, each bicopter assumes a state with relatively low yaw rates—the state substantially deviated from its hovering condition. This significantly deteriorates the effectiveness of the flight controller that is derived based on the hovering solution, making the robot temporarily lose some degree of stability. To overcome this, an undocking structure with a preloaded catapult mechanism is designed and fabricated. The mechanism initially keeps two bicopters together as a quadcopter for flight. When activated, the contraction of a shape memory alloy (SMA) releases the bicopter and simultaneously converts the stored elastic energy into the rotational kinetic energy of both bicopters. The undocking mechanism impulsively provides the bicopters with sufficient initial yaw speeds, assisting them to quickly reach their hovering states. As a result, the disassembly can be reliably accomplished even at a low flight altitude. It can be seen that the complexity of the transition process of SplitFlyer Air surpasses those of previous modular MAVs [10], [14], [32] as the procedure extends beyond pure physical attachments.

This paper is organized as follows. Section II details the concept and fabricated prototypes of SplitFlyer Air. This includes the design and modeling of the undocking mechanism. In Section III, the flight dynamics of both quadcopters and bicopters are given under the same framework. The analysis considers reduced attitude dynamics through consideration of the angular momentum of the platforms. A flight control method suitable for both operational modes, with minor differences in the mapping of control inputs, is proposed in Section IV. The experiments, including the performance evaluation of the undocking mechanism, trajectory tracking flights and the demonstration of the mid-air disassembly are described in Section V. Lastly, a conclusion is provided.

II. Split Quadcopter Platform

A. Modular Multirotor Robot Design

SplitFlyer Air is a modular transformable multirotor robot. As shown in Fig. 1a, the quadcopter is constructed from two bicopters as base units. Each bicopter module features a pair of clockwise (CW) or counterclockwise (CCW) propellers. The differences between the two units are the propellers' spinning directions and the two-part interlocking mechanism that allows both modules to be attached or disengaged. The flight modules are referred to as Bicopter-CW and Bicopter-CCW according to the type of equipped propellers as illustrated in Fig. 1b.

With the proposed design, SplitFlyer Air has two modes of aerial locomotion. In the quadcopter form (Fig. 1a), the robot is equipped with four brushless motors and functions as a conventional multirotor vehicle. Nevertheless, the platform includes two sets of flight controllers, power electronics, and airframes. Once transformed, the robot splits into two bicopters that can independently perform controlled flight despite being severely underactuated.

In the bicopter configuration, due to the non-zero aerodynamic torque produced by two propellers with the same spinning direction, the bicopter maintains a relatively high yaw rate in flight. This motivates us to regard the robot as a spinning disk to radically simplify the dynamics modeling and controller design. In order to meet the imposed condition, each bicopter carries two batteries that are strategically placed to obtain symmetrical mass distribution, which leads to the approximately axisymmetric distribution of the moment of inertia about the yaw axis as intended.

One principal difficulty in the realization of the proposed transformable vehicle is the reconciliation of two flight modes during the mid-air transition. As aforementioned, in contrast to a conventional quadcopter, the bicopters fly with a high revolving rate during hover. Immediately after the disassembly, each bicopter must quickly build up its yaw rate to reach its hovering state. During this period, the robot briefly loses some altitude and its ability to fully control its attitude. To shorten the temporary loss of control, the SMA-actuated elastic catapult mechanism is developed. Exploiting the elastic energy stored in the preloading step, the two-part mechanism shown in Fig. 2b and c not only enables two bicopters to instantaneously undock when triggered, but also impulsively provides substantial initial angular momentum to both robots, assisting them to acquire the fast revolving rates required for hovering quickly. Thanks to the catapult-like undocking mechanism, SplitFlyer Air is capable of performing a mid-air transformation in tight volume, marking a major milestone from the preliminary prototype in [25] that necessitates human assistance to manually perform the reconfigurations.

B. SplitFlyer Air Prototypes

For each bicopter module, the all-in-one flight control board (Bitcraze Crazyflie Bolt) was employed and placed at the center of the airframe. The airframes with 20-cm wheelbase, also acting as a protective ring, were machined from 3-mm-thick carbon fiber sheets. For the propulsion system, 5×3-inch two-blade propellers were paired with 2300KV 2204 brushless motors with built-in electronic speed controllers (ESC). Compared with our previous prototype [25], the increased size reduces the proportion of the weight of the flight controller board to the vehicle weight from 30% to 4%, raising the available payload budget for the undocking mechanism.

For each bicopter unit, two 550mAh 3s Li-ion batteries were diagonally installed as captured in Fig. 1. This arrangement guarantees that the bicopter has even mass and inertia distribution as assumed for the modeling purposes so that the bicopter can be dynamically treated as a gyroscope (detailed in Section III). The mass of Bicopter-CCW and Bicopter-CW are 310.4 g and 366.8 g, with the difference primarily attributed to the upper and lower parts of the undocking mechanism (9.6 g and 66.0 g). The estimated moment of inertia (by CAD software, Fusion 360) of the bicopter about its roll ($\hat{\mathbf{x}}_b$), pitch ($\hat{\mathbf{y}}_b$), and yaw ($\hat{\mathbf{z}}_b$) axes are $I_x = 1.56\times10^4$, $I_z = 1.56\times10^4$, and $I_z = 3.07\times10^4$ g·cm^2 (the relatively lightweight undocking mechanism is centrally located and not taken into consideration in the calculation).

The SMA-actuated undocking mechanism, of which the design and working principle are described below, was fabricated from 3D printed components (Formlabs Form 3, gray resin v4), commercially available bearings, and carbon fiber rods. The two-part mechanism are assembled on the two bicopters. The SMA wire (MuscleWires Flexinol LT, 125 μm) is driven by a separate ultra compact motor driver (HR8833) that receives the command from an onboard GPIO pin on the Crazyflie Bolt belonging to Bicopter-CW.

C. Undocking Mechanism

To enable the Splitflyer Air to autonomously transform into two bicopters mid-air, the robot needs a set of undocking mechanism with an active trigger function. In this work, we designed a preloaded catapult mechanism that allows two bicopters to efficiently undock when commanded. The mechanism, as visible in Fig. 1, is schematically broken down in Fig. 2. With the preload, the mechanism rigidly locks the bicopters together, preventing an accidental disassembly. Once prompted, the SMA contraction unlatches the two bicopters and converts the stored elastic energy to provide the bicopters initial revolving motion required for their flights.

1) Mechanical design: The undocking mechanism is divided into the docking head and the catapult mechanism as illustrated in Fig. 2a. The docking head resides directly underneath Bicopter-CCW and the catapult mechanism is attached on top of Bicopter-CW as shown in Fig. 1. The mechanism integrates elastic elements (rubber bands) that takes the motivation from a clockwork device. In the initial docking process via a human operator, the elastic elements are stretched as preload. The coupled four-bar and latching mechanism tightly lock the docking head and the catapult mechanism together. When the SMA is triggered, the mechanism is unlatched and the stored energy is released as rotational kinetic energy to supply the bicopters with initial rotational rates as seen in the supplementary video. The details are given as follows.

The catapult mechanism is comprised of four-bar linkages (the yellow parts in Fig. 2a, ⑧ and ⑨, also visible in the supplementary video), a rotational wheel (the green part in Fig. 2a, ④) and the mechanical ground (the gray part in Fig. 2a, ③). The wheel is assembled on the center of the supporting structure and supported by two nylon bearings (only one bearing is visible in Fig. 2a, ①). Such design provides rigidity for the wheel so that it does not tilt from the axis when subject to force or torque. There are two hooks on the opposite sides of the wheel (② in Fig. 2a and b) for installations of the elastic elements (rubber bands, not shown in Fig. 2a, see Fig. 2b).

To apply the preload, the docking head is brought into contact with the wheel while the structural component of the catapult mechanism is fixed. Four pairs of interlocking features on the docking head and the wheel (⑤ in Fig. 2a) synchronize

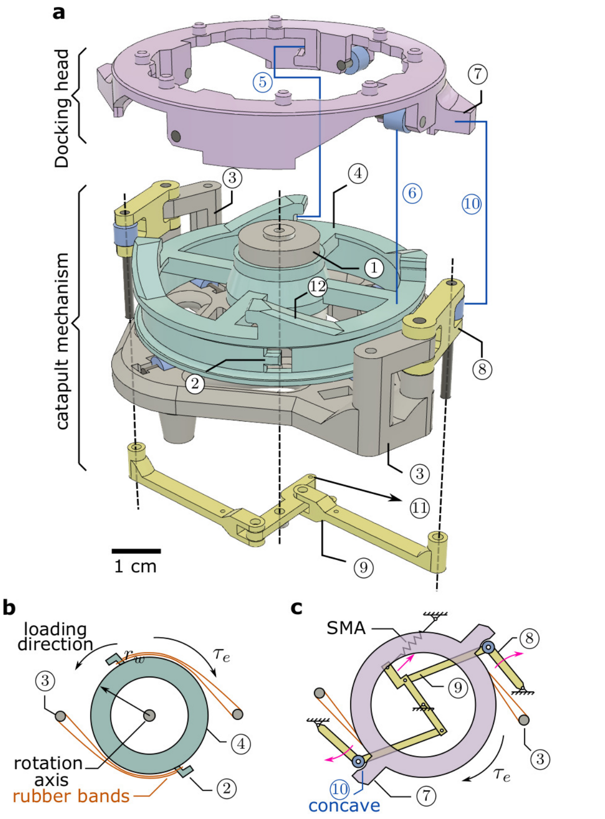

Fig. 2. The undocking mechanism. (a) A 3D CAD drawing of the two-part mechanism. The dashed lines indicate alignment axes. The docking head residing underneath Bicopter-CCW is fastened to the catapult mechanism located on top of Bicopter-CW to form SplitFlyer Air. (b) A diagram of the rubber band-based elastic energy storage mechanism. (c) A schematic of the coupled four-bar linkages that transmit the SMA actuation to disengage the interlocking mechanism and undock the bicopters from each other.

the anticlockwise rotation of the docking head (produced by the operator) with the wheel while still allowing the docking head to rotate freely in the opposite direction. This directional coupling facilitates the undocking process described in the subsequent paragraphs. Through the anticlockwise rotation of the head and the wheel, the elastic bands located in the chute along the outer diameter of the wheel are elongated. As a result, the wheel together with the elastic elements act as the energy storage device (Fig. 2b). To keep the elastic bands in tension, two protruding tabs (⑦ in Fig. 2a and c) on the docking head and two corresponding links on the catapult structure (⑧ in Fig. 2a and c) form two sets of interlocking mechanisms to prevent the back rotation when engaged, keeping the mechanism loaded. The concave face of the protruding tab (⑩ in Fig. 2c) serves as a groove that retains the rounded end of the four-bar linkages in place. The restoring torque τ_e generated by the stretched elastic bands securely keeps the docking head (and the wheel) in place with respect to the mechanical ground in the locked state.

To disengage the mechanism in flight, the SMA is triggered and contracted under the generated heat. The contraction is propagated through the coupled four-bar linkages as indicated by magenta arrows in Fig. 2c (see also the supplementary video). The contraction force overcomes the friction and restoring torque, unlatching both locks simultaneously. Accordingly, the stored elastic energy is released, producing the action and reaction torque τ_e that rotates the wheel and the docking head in the clockwise direction with respect to the catapult platform. The motion continues beyond the point where the fasteners (⑤) between the docking head and wheel are separated. Owing to the inertia of both bicopters, at this stage, the docking head starts to build up a non-zero (clockwise) rotational rate with respect to the wheel. This relative rotation is facilitated by the inclusion of four micro bearings (blue cylinders, ⑥ in Fig. 2a) underneath the head. Once these bearings reach the slanted faces on the wheel (⑫), the surface normal pushes the docking head away from the catapult platform, separating two bicopters from each other.

2) Analysis of elastic energy and disengagement speed: For the outlined catapult mechanism, the rotational speeds of the docking components when they are separated depend primarily on the elastic energy stored during the preload. Under simplified conditions, neglecting the viscous loss and friction from the multi-layer winding on the wheel, the elastic energy can be equated with the kinetic energy associated with the rotation of the bicopters when they are separated.

To compute the potential energy stored during the preload, we let $f_e = f_e(l_e)$ be the restoring force profile of an elastic band when l_e is the amount of the elongation. The elongation can also be expressed as the product of the wheel radius $r_w = 27.5$ mm and the angular displacement θ_e from the preloading process. With n elastic bands mounted, the potential energy stored in the catapult mechanism is

$$U(\theta_e) = n r_w \int_0^{\theta_e} f_e(r_w \theta)\,\mathrm{d}\theta. \quad (1)$$

Ignoring viscous losses and translational kinetic energy, the potential energy is equally transferred to the angular kinetic energy of two bicopters, producing the initial rotational speed immediately after the undocking as

$$\omega_i(\theta) = \sqrt{U(\theta_e)/I_z}, \quad (2)$$

where I_z denotes the bicopter's yaw moment of inertia. The result is used to model and estimate ω_i of the fabricated prototype in Section V-A2.

III. Bimodal Flight Dynamics

The proposed vehicle has two modes of aerial locomotion: quadcopter and bicopter modes. Although these two configurations are different in flight principles, both robots can be treated as rigid bodies equipped with thrusters that are aligned with the robot's $\hat{\mathbf{z}}_b$ axis. As a consequence, their flight dynamics can be predominantly captured by a single set of equations of motion.

A. Translational Dynamics

To describe the translational dynamics of a bicopter or a quadcopter, we consider the robot as a rigid body with mass m equipped with four or two propellers in the gravity field, as illustrated in Fig. 3a. The diagram displays all four rotor's thrusts ($\mathbf{f}_1$ to $\mathbf{f}_4$) belonging to the quadcopter. For a bicopter,

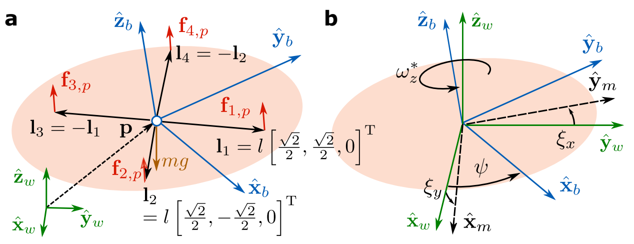

Fig. 3. Schematic diagrams illustrating the flight dynamics of the robots. (a) The definitions of the inertial frame and body-fixed frames. The airframe (of the quadcopter or bicopters) is drawn in light blue with a blue dot denoting the center of mass. The propeller axes are shown with red arrows. (b) In flight, a bicopter flies with a high yaw rate and, hence, is abstracted as a spinning disk for modeling and control purposes. The inertial frame ($\hat{\mathbf{x}}_w\hat{\mathbf{y}}_w\hat{\mathbf{z}}_w$) is falsely drawn on top of the body frame ($\hat{\mathbf{x}}_b\hat{\mathbf{y}}_b\hat{\mathbf{z}}_b$) for clarity. A non-revolving frame ($\hat{\mathbf{x}}_m\hat{\mathbf{y}}_m\hat{\mathbf{z}}_b$) with the associated angles of inclination ξ_x and ξ_y is introduced to describe the attitude of the disk.

the $\mathbf{f}_1$ and $\mathbf{f}_3$ pair or $\mathbf{f}_2$ and $\mathbf{f}_4$ pair are disregarded depending on the bicopter configuration (CCW or CW, refer to Fig. 1). Frame $\hat{\mathbf{x}}_b\hat{\mathbf{y}}_b\hat{\mathbf{z}}_b$ denotes the body-fixed frame located on the center of mass of each robot. Let $\mathbf{p} = [x, y, z]^{\mathrm{T}}$ represent the position of the robot in the inertial frame ($\hat{\mathbf{x}}_w\hat{\mathbf{y}}_w\hat{\mathbf{z}}_w$), and g to be the gravitational constant, the translational motion of the robot is given by

$$m\ddot{\mathbf{p}} = \mathbf{R}\sum_i \mathbf{f}_i - mg\mathbf{e}_3, \tag{3}$$

where, $\mathbf{R} \in \mathrm{SO}(3)$ is a rotation matrix mapping the body frame to the inertial frame. $\mathbf{e}_3 = [0, 0, 1]^{\mathrm{T}}$ is a basis vector, $\mathbf{f}_i$ is the force associated with the i^{th} propeller. The summation is for $i = 1, 3$ for Bicopter-CW and $i = 2, 4$ for Bicopter-CCW and $i = 1, 2, 3, 4$ for the quadcopter as indicated earlier. The force $\mathbf{f}_i$ is generally taken as the thrust produced by the propeller, aligned with $\hat{\mathbf{z}}_b$ as $\mathbf{f}_i = \mathbf{e}_3 f_{i,p}$. However, in the case of flight with a significant body-centric rotational speed ($\boldsymbol{\omega}$), in which the propellers travel with a substantial speed with respect to still air, the induced drags $\mathbf{f}_{i,d}$ of the propeller becomes non-negligible. This results in

$$\mathbf{f}_i = \mathbf{e}_3 f_{i,p} + \mathbf{f}_{i,d}. \tag{4}$$

Modeled by blade element momentum theory [33] and empirically verified in [27], [28], the induced drag of the i^{th} rotor is linearly proportional to its translational velocity $\mathbf{v}_i$. For rotating robots, $\mathbf{v}_i$ is attributed to the projected vehicle's velocity $\mathbf{R}^{-1}\dot{\mathbf{p}}$ and the body rotation $\boldsymbol{\omega} \times \mathbf{l}_i$, where $\mathbf{l}_i$ is the location of the i^{th} propeller in the body frame. This yields

$$\mathbf{f}_{i,d} = -\mathbf{B}\mathbf{v}_i = -\mathbf{B}\mathbf{R}^{-1}\dot{\mathbf{p}} - \mathbf{B}\boldsymbol{\omega} \times \mathbf{l}_i, \tag{5}$$

with $\mathbf{B} = \mathrm{diag}\left(B_h, B_h, B_v\right)$ being a diagonal matrix representing the drag coefficients [28]. (5) states that the rotor drag is caused by both the robot's translation and rotation, but for bicopter robots the rotation term is dominant as $|\boldsymbol{\omega} \times \mathbf{l}_i| \gg |\dot{\mathbf{p}}|$. To compute the total force contributed by all propellers (in the inertial frame), we substituting $\mathbf{f}_i$ into (3) using (4) and (5). This produces

$$\mathbf{R}\sum_i \mathbf{f}_i = \mathbf{R}\mathbf{e}_3\sum_i f_{i,p} - \mathbf{R}\mathbf{B}\mathbf{R}^{-1}\dot{\mathbf{p}}\sum_i 1. \tag{6}$$

It turns out that the terms associated with $\boldsymbol{\omega}$ disappear due to the symmetry of the vehicle ($\mathbf{l}_1 = -\mathbf{l}_3 = l\left(\hat{\mathbf{x}}_b + \hat{\mathbf{y}}_b\right)/\sqrt{2}$ and $\mathbf{l}_2 = -\mathbf{l}_4 = l\left(\hat{\mathbf{x}}_b - \hat{\mathbf{y}}_b\right)/\sqrt{2}$ as illustrated in Fig. 3). The term associated with $\dot{\mathbf{p}}$ in (6) is, in fact, present in all multitor vehicles, nevertheless, it is often neglected unless the vehicle undergoes aggressive maneuvers [21], [23], [26], [34]. As a result, (3) reduces to

$$m\ddot{\mathbf{p}} = \mathbf{R}\mathbf{e}_3\sum_i f_{i,p} - mg\mathbf{e}_3. \tag{7}$$

The result implies that, despite the presence of notable angular rates, the translational dynamics of the bicopters or quadcopter is independent of its angular velocity $\boldsymbol{\omega}$.

B. Attitude Dynamics

As a rigid body, the robot's attitude dynamics in the body frame are captured by Euler's equations:

$$\mathbf{I}\dot{\boldsymbol{\omega}} + \boldsymbol{\omega} \times \mathbf{I}\boldsymbol{\omega} = \sum_i \boldsymbol{\tau}_i + \boldsymbol{\tau}_s, \tag{8}$$

where, $\mathbf{I} = \mathrm{diag}\left(I_x, I_y, I_z\right)$ is the inertia moment of the vehicle (bicopters or quadcopter), $\boldsymbol{\tau}_s = -\mathbf{D}\boldsymbol{\omega}$ denotes the linear aerodynamic body damping term with $\mathbf{D} = \mathrm{diag}\left(D_h, D_h, D_v\right)$ (owing to the symmetry of the robots). In (8), $\boldsymbol{\tau}_i$ is the torque produced by the propelling thrust and the rotor's drag $\mathbf{f}_i = \mathbf{e}_3 f_{i,p} + \mathbf{f}_{i,d}$ from (4), combined with the thrust-induced torque. Therefore,

$$\begin{aligned} \boldsymbol{\tau}_i &= \mathbf{l}_i \times \mathbf{f}_i + \delta_i \kappa f_{i,p}\mathbf{e}_3, \\ &= \mathbf{l}_i \times \left(\mathbf{e}_3 f_{i,p} + \mathbf{f}_{i,d}\right) + \delta_i \kappa f_{i,p}\mathbf{e}_3, \end{aligned} \tag{9}$$

where κ is the propeller specific thrust-to-drag ratio and $\delta_i = (-1)^{i-1}$ distinguishes the clockwise and counterclockwise spinning propellers. In total, (8) captures the rotational dynamics in the body frame, taking into account the aerodynamic dampings from the spinning propellers and rotating body.

C. Hovering Solution

To gain fundamental insights into the flight principles, we consider the conditions that lead to a hovering state, defined as $\dot{\mathbf{p}}, \ddot{\mathbf{p}} = \mathbf{0}$ and $\dot{\boldsymbol{\omega}} = \mathbf{0}$. According to the translational dynamics from (7), the hovering state (denoted by $\cdot^*$) necessitates

$$\mathbf{R}^*\mathbf{e}_3 = \mathbf{e}_3 \quad \text{and} \quad \sum_i f_i^* = mg. \tag{10}$$

The condition implies that the robot stays upright ($\omega_x^*, \omega_y^* = 0$) with a constant yaw rate ω_z^* depending on the interplay between the induced torque of propellers and the total rotational drag. For the case of the bicopters, which possess two propellers with the same spinning direction, they can only achieve a particular non-zero constant revolving speed $\omega_z^* = \delta_i \kappa mg/(\sum_i B_h l^2 + D_v)$.. On the contrary, a quadcopter is able to hold an arbitrary constant revolving speed ω_z^* by correspondingly adjusting the sum of propellers' torque under the constraint $\sum_i f_i^* = mg$.

D. Gyroscopic Motion and Reduced Flight Dynamics

According to the hovering state determined in Section III-C, non-aggressive bicopter and quadcopter flights are both accomplished near the nominally upright orientation $\hat{\mathbf{z}}_b^* = \mathbf{e}_3$ with an approximately constant yaw rate or $\dot{\omega}_z \approx 0$. This encourages us to analyze the robot's dynamics near this nominal state. The following models are developed based on the assumption that the deviation of the robot's attitude state from its equilibrium point $\hat{\mathbf{z}}_b^* = \mathbf{e}_3$ is small. Thus we let

$$\hat{\mathbf{z}}_b \approx \begin{bmatrix} \xi_y & -\xi_x & 1 \end{bmatrix}^{\mathrm{T}} \quad \text{with} \quad |\xi_x|, |\xi_y| \ll 1. \tag{11}$$

1) Near-hovering translational dynamics: Under the notation introduced by (11), the translational dynamics from (7) can be integrated with the approximate force equilibrium constraint from (10) and broken into the horizontal and vertical components as

$$m\ddot{\mathbf{p}}_2 = mg\mathbf{J}\boldsymbol{\xi} \quad \text{and} \quad m\ddot{z} = \sum_i f_{i,p} - mg, \tag{12}$$

where $\boldsymbol{\xi} = [\xi_x, \xi_y]^{\mathrm{T}}$. $\mathbf{p}_2 = [x, y]^{\mathrm{T}}$ is the 2×1 vector of the horizontal position (different from the 3×1 vector $\mathbf{p}$), and $\mathbf{J}$ is a 2×2 skew-symmetric matrix with unit determinant equal to the -90°-rotation matrix. These equations are later used for the design of a flight controller for non-aggressive trajectories.

2) Reduced attitude dynamics: The attitude dynamics are revisited by abstracting the robot as an angular momentum object in the inertial frame. Compared to the conventional body-frame centric approach, the inertial frame consideration is suitable for vehicles that are severely underactuated with a large yaw rate including the bicopters.

As explained in Section II-B, the vehicle's mass distribution is approximately axisymmetric by design. That is, its moment of inertia about the pitch and roll axes are approximately equal or $\mathbf{I} = \mathrm{diag}(I_d, I_d, I_z)$, this permits the robot to be seen as an axisymmetric gyroscope. Referring to Fig. 3b (which depicts the robot as a disk), we may define a coordinate frame $\hat{\mathbf{x}}_m\hat{\mathbf{y}}_m\hat{\mathbf{z}}_b$ with $\hat{\mathbf{x}}_m \approx [1, 0, -\xi_y]^{\mathrm{T}}$ and $\hat{\mathbf{y}}_m \approx [0, 1, \xi_x]^{\mathrm{T}}$ to highlight the direction of $\hat{\mathbf{z}}_b$ in the inertial frame, irrespective of the actual yaw angle ψ. In this setting, the angular momentum of the robot in the inertial frame is

$$\mathbf{L} = I_d\dot{\xi}_x\hat{\mathbf{x}}_m + I_d\dot{\xi}_y\hat{\mathbf{y}}_m + I_z\Omega_z^*\hat{\mathbf{z}}_b. \tag{13}$$

Using the fact that $\dot{\hat{\mathbf{x}}}_m = -\dot{\xi}_y\hat{\mathbf{z}}_b$, $\dot{\hat{\mathbf{y}}}_m = \dot{\xi}_x\hat{\mathbf{z}}_b$, and $\dot{\hat{\mathbf{z}}}_b = \dot{\xi}_y\hat{\mathbf{x}}_m - \dot{\xi}_x\hat{\mathbf{y}}_m$, the reduced attitude dynamics are obtained by taking the time derivative of (13) [35]. With some algebraic manipulation, this yields

$$I_d\ddot{\boldsymbol{\xi}} + I_z\Omega_z^*\mathbf{J}\dot{\boldsymbol{\xi}} = [\mathbf{e}_1, \mathbf{e}_2]^{\mathrm{T}} \mathbf{R} \left(\sum_i \boldsymbol{\tau}_i + \boldsymbol{\tau}_s \right) = \boldsymbol{\tau}_w + \boldsymbol{\tau}_d \tag{14}$$

where the collective torque on the right-hand side, corresponding to $\dot{\mathbf{L}}$, is taken from (8) and (9) with the projection on to the $\hat{\mathbf{x}}_w$ and $\hat{\mathbf{y}}_w$ directions through the basis vectors $\mathbf{e}_1 = [1, 0, 0]^{\mathrm{T}}$ and $\mathbf{e}_2 = [0, 1, 0]^T$. The contribution from $f_{i,p}$, $\boldsymbol{\tau}_w$, is defined to be $\boldsymbol{\tau}_w = [\mathbf{e}_1, \mathbf{e}_2]^{\mathrm{T}} \mathbf{R} \sum_i \mathbf{l}_i \times f_{i,p}\mathbf{e}_3$, whereas the rest (the terms associated with $\mathbf{f}_{i,d}$ and $\boldsymbol{\tau}_s$ from (5) and (8)) is lumped into $\boldsymbol{\tau}_d$. For small deviations $|\xi_x|, |\xi_y| \ll 1$, the rotation matrix is approximated as $\mathbf{R} \approx \mathbf{R}_z(\psi)$ to capture the instantaneous yaw state of the robot (see Fig. 3b). Furthermore, it can be shown that $[\mathbf{e}_1, \mathbf{e}_2]^{\mathrm{T}} \mathbf{R}_z(\psi) \mathbf{D}\boldsymbol{\omega} = D_h\dot{\boldsymbol{\xi}}$. Therefore,

$$\begin{aligned} \boldsymbol{\tau}_d = &- [\mathbf{e}_1, \mathbf{e}_2]^{\mathrm{T}} \mathbf{R}_z(\psi) \sum_i \mathbf{l}_i \times \left(\mathbf{B}\mathbf{R}^{-1}\dot{\mathbf{p}} + \mathbf{B}\boldsymbol{\omega} \times \mathbf{l}_i \right) \\ &- D_h\dot{\boldsymbol{\xi}}. \end{aligned} \tag{15}$$

To further simplify $\boldsymbol{\tau}_d$, we apply the fact that $\mathbf{l}_1 = -\mathbf{l}_3 = l(\hat{\mathbf{x}}_b + \hat{\mathbf{y}}_b)/\sqrt{2}$ and $\mathbf{l}_2 = -\mathbf{l}_4 = l(\hat{\mathbf{x}}_b - \hat{\mathbf{y}}_b)/\sqrt{2}$ (by design) and $\dot{\boldsymbol{\xi}} = \mathbf{R}_2^{\mathrm{T}}(\psi)[\mathbf{e}_1, \mathbf{e}_2]^{\mathrm{T}}\boldsymbol{\omega}$ with $\mathbf{R}_2(\cdot)$ being a 2×2 rotation matrix. The sum of $\dot{\mathbf{p}}$-dependent terms in (15) becomes zero. That is, the translation of the vehicle does not directly affect the reduced attitude dynamics. Subsequently, (15) reduces to

$$\boldsymbol{\tau}_d = \frac{1}{2} \sum_i B_v l^2 \delta_i \begin{bmatrix} \sin 2\psi & \cos 2\psi \\ \cos 2\psi & \sin 2\psi \end{bmatrix} \dot{\boldsymbol{\xi}} - D_\xi\dot{\boldsymbol{\xi}}, \tag{16}$$

in which $D_\xi = \frac{1}{2}\sum_i B_v l^2 + D_h$ is defined as a lumped rotational damping coefficient. The first term in (16) is dependent on the yaw angle ψ. For a quadcopter, ψ is likely slowly time-varying. Its contribution to $\boldsymbol{\tau}_d$ can be easily marginalized out by the flight controller. For a bicopter with $\dot{\psi} \approx \omega_z^*$, the first term in (16) becomes a zero-mean fast oscillatory signal which can be neglected, leaving $\boldsymbol{\tau}_d \approx -D_\xi\dot{\boldsymbol{\xi}}$.

Meanwhile, the control input for the reduced attitude dynamics, $\boldsymbol{\tau}_w$ from (14), can be controlled independently for the case of a quadcopter. For the case of the bicopter robots, however, $\boldsymbol{\tau}_w$ cannot be controlled independently because of the severe underactuation. Based on the frame definitions shown in Fig. 1b, the portion of the torque directly attributed to the propelling thrust can be written as

$$\boldsymbol{\tau}_w = \frac{l}{\sqrt{2}}(f_{j,p} - f_{j+2,p})\left((-1)^{j+1}\mathbf{1} + \mathbf{J}\right)\begin{bmatrix} \cos\psi \\ \sin\psi \end{bmatrix} \tag{17}$$

in which $j = 1$ for Bicopter-CW and $j = 2$ for Bicopter-CCW, and $\mathbf{1}$ is an identity matrix. (17) states that $\boldsymbol{\tau}_w$ is determined from the difference between two propelling forces $(f_{j,p} - f_{j+2,p})$ and ψ for the bicopters. The dependence on ψ means $\boldsymbol{\tau}_w$ has one degree of freedom cannot be arbitrarily commanded. This is different from a conventional quadcopter.

IV. Flight Controller

As shown in Section III, apart from the issue of underactuation of bicopters, flight dynamics of both bicopters and quadcopters can be largely expressed with the same models. This encourages us to develop a single control method for both modes. To achieve this, we devise the controller based on the near-hovering dynamics by considering the vertical and horizontal translations of the robots, taking into account the reduced attitude dynamics. Unlike the early development in [25] and related works [21]–[24], the flight controller here does not rely on the timescale separation between the attitude and translational dynamics that gives rise to cascaded control loops. This results in improved tracking ability. Finally, the torque generation method for bicopters based on cyclic commands is provided to workaround the severe underactuation of the bicopter platform.

A. Altitude Control

Based on the near-hovering dynamics described by (12), the altitude dynamics of the robot can be considered independently from other modes. As a linear second-order system, a standard proportional–integral–derivative (PID) control law guarantees the convergence. For a given setpoint trajectory $z_r(t)$, the total required thrust $f_{i,r}$ is computed from

$$\sum_i f_{i,r} = m\ddot{z}_r - k_{z,p}\tilde{z} - k_{z,d}\dot{\tilde{z}} - k_{z,i}\int \tilde{z}\mathrm{d}t + mg, \quad (18)$$

where $\tilde{z} = z - z_r$ denotes the altitude error and $k_{z,(\cdot)}$'s are control gains. The closed-loop stability is achieved when k_z's satisfy the Routh-Hurwitz stability criterion. Note that the method is suitable for both quadcopter and bicopters by applying different sets of parameters.

B. Horizontal Position Control

The horizontal position controller is devised based on the assumption that the bicopter or quadcopter is able to arbitrarily generate torque about $\hat{\mathbf{x}}_m$ and $\hat{\mathbf{y}}_m$ axes at any instance, although this is not entirely the case for the bicopters. The violation is later addressed in Section IV-C2.

Given the lateral reference trajectory $\mathbf{p}_r = [x_r, y_r]^{\mathrm{T}}$, the position error is defined as $\tilde{\mathbf{p}} = \mathbf{p}_2 - \mathbf{p}_r$. The following constraint is employed for the construction of the control law

$$\tilde{\mathbf{p}}^{(4)} + \lambda_3\tilde{\mathbf{p}}^{(3)} + \lambda_2\ddot{\tilde{\mathbf{p}}} + \lambda_1\dot{\tilde{\mathbf{p}}} + \lambda_0\tilde{\mathbf{p}} = 0, \quad (19)$$

where $\tilde{\mathbf{p}}^{(i)}$ indicates the i^{th}-order time derivative of $\tilde{\mathbf{p}}$ and λ's are positive scalar gains. The convergence of $\tilde{\mathbf{p}}$ is guaranteed when λ's satisfy the Routh-Hurwitz criterion. The derivatives of the error terms are evaluated from (12), (14) and (15):

$$\begin{aligned} \ddot{\tilde{\mathbf{p}}} = g\mathbf{J}\boldsymbol{\xi} - \ddot{\mathbf{p}}_r, \quad \tilde{\mathbf{p}}^{(3)} = g\mathbf{J}\dot{\boldsymbol{\xi}} - \mathbf{p}_r^{(3)}, \quad (20) \\ \tilde{\mathbf{p}}^{(4)} = \mathbf{J}\frac{g}{I_d}\left(\boldsymbol{\tau}_w - D_\xi\dot{\boldsymbol{\xi}} - I_z\omega_z^*\mathbf{J}\dot{\boldsymbol{\xi}}\right) - \mathbf{p}_r^{(4)}. \end{aligned}$$

It can be seen that the control input $\boldsymbol{\tau}_w$ emerges from the term $\tilde{\mathbf{p}}^{(4)}$. Therefore, the control law for $\boldsymbol{\tau}_w$, notated as $\boldsymbol{\tau}_{w,r}$ is obtained based on the feedback of $\mathbf{p}_2$, $\boldsymbol{\xi}$, and their derivatives. This yields a single input for controlling the entire system encompassing both attitude and translational dynamics. Observe that the term $\mathbf{p}_r^{(4)}$ in (20) serves as the feedforward command. This allows the robot to follow dynamic and aggressive trajectories more accurately. For improved clarity, we provide a state-space representation of the system and a block diagram of the control architecture in Section S1. For the actual implementation, $\boldsymbol{\tau}_{w,r}$ must be translated to the propeller commands f_i's according to individual platforms as discussed below.

C. Mapping of Control Inputs

1) Implementation on quadcopter: To apply (19) to a quadcopter, a yaw controller to guarantee the prerequisite of $\dot{\omega}_z \approx 0$ is needed. For a given yaw trajectory $\psi_r(t)$ with $\ddot{\psi}_r \approx \dot{\omega}_z \approx 0$, the yaw error $\tilde{\psi} = \psi - \psi_r$ is minimized with a PID scheme

$$\sum_i \delta_i\kappa f_{i,r} = I_z\ddot{\psi}_r - k_{\psi,p}\tilde{\psi} - k_{\psi,d}\dot{\tilde{\psi}} - k_{\psi,i}\int \tilde{\psi}\mathrm{d}t, \quad (21)$$

where $k_{z,(\cdot)}$'s are control gains. Thereafter, all control laws from (18), (19), and (21) are consolidated. The laws provide four linear constraints that allow the thrust of all four propellers $f_{i,r}$ to be computed in a similar manner to conventional quadcopter control methods [26].

In summary, the proposed flight controller, when combined with a simple yaw regulator, can be used to control a quadcopter with a small $\dot{\omega}_z$. When $\omega_z = 0$, the method can be seen as a non-cascaded controller derived from the linearized dynamics similar to the strategy used in [36].

2) Implementation on bicopters: Up until (20), the flight dynamics of a bicopter and a quadcopter have been universally elaborated by a single set of equations. Herein, we seek to realize the control torque $\boldsymbol{\tau}_{w,d}$ set by (20) for position control of the bicopter and simultaneously meet the condition for altitude controller from (18).

Together, the total thrust $\sum_i f_{i,r}$ determined by the altitude controller and the desired torque $\boldsymbol{\tau}_{w,r}$ for regulation of the horizontal position constitute three constraints. These cannot be concurrently realized as the bicopters are only equipped with two independent actuators. To overcome the severe under-actuation, we exploit the inherently fast yaw rate to control the robot in a cycle-averaged manner. To elaborate, we determine the force commands using the following equations:

$$\begin{aligned} f_{j,r} + f_{j+2,r} &= \ddot{z}_r - k_{z,p}\tilde{z} - k_{z,d}\dot{\tilde{z}} - k_{z,i}\int \tilde{z}\mathrm{d}t + mg, \\ f_{j,r} - f_{j+2,r} &= \frac{\sqrt{2}}{l}\boldsymbol{\tau}_{w,r}^{\mathrm{T}}\left((-1)^{j+1}\mathbf{1} + \mathbf{J}\right)\begin{bmatrix} \cos\psi \\ \sin\psi \end{bmatrix}. \quad (22) \end{aligned}$$

The first condition directly follows the altitude control law (18), whereas the second condition is an attempt to realize the horizontal position control (19). When this is substituted into (17), we obtain

$$\begin{aligned} \boldsymbol{\tau}_w = \boldsymbol{\tau}_{w,r}^{\mathrm{T}}\left((-1)^{j+1}\mathbf{1} + \mathbf{J}\right)\begin{bmatrix} \cos\psi & \sin\psi \end{bmatrix}^{\mathrm{T}} \\ \left((-1)^{j+1}\mathbf{1} + \mathbf{J}\right)\begin{bmatrix} \cos\psi & \sin\psi \end{bmatrix}^{\mathrm{T}}, \quad (23) \end{aligned}$$

which eventually leads to

$$\begin{aligned} \boldsymbol{\tau}_w &= \boldsymbol{\tau}_{w,r} + (-1)^{j+1}\begin{bmatrix} \sin 2\psi & -\cos 2\psi \\ -\cos 2\psi & \sin 2\psi \end{bmatrix}\boldsymbol{\tau}_{w,r} \\ &= \boldsymbol{\tau}_{w,r} + \Delta\boldsymbol{\tau}_{w,r}, \quad (24) \end{aligned}$$

where we have defined $\Delta\boldsymbol{\tau}_{w,r}$ to represent the leftover torque with fast dynamics ($\dot{\psi} = \omega_z$) and zero bias. The mean of $\Delta\boldsymbol{\tau}_{w,r}$ is zero when averaged over a cycle. Regarding $\Delta\boldsymbol{\tau}_{w,r}$ as the high-frequency disturbance, the implementation of (22) approximately steers $\boldsymbol{\tau}_w$ to $\boldsymbol{\tau}_{w,r}$ as desired.

To mitigate the impact of $\Delta\boldsymbol{\tau}_{w,d}$ on the closed-loop stability, we let $P(s)$ represent the transfer function of the reduced attitude dynamics in the vicinity of the hovering state (derived from (14), s is the Laplace variable). This $P(s)$ models the actual dynamics of $\boldsymbol{\xi}$ belonging to the bicopter in flight. With the result from (24), we anticipate

$$\boldsymbol{\xi}(s) = P(s)\boldsymbol{\tau}_w(s) = P(s)\boldsymbol{\tau}_{w,r}(s) + P(s)\Delta\boldsymbol{\tau}_{w,r}(s), \quad (25)$$

which indicates the presence of a high-frequency oscillation excited by the term $\Delta\boldsymbol{\tau}_{w,r}$. To attenuate the influence of

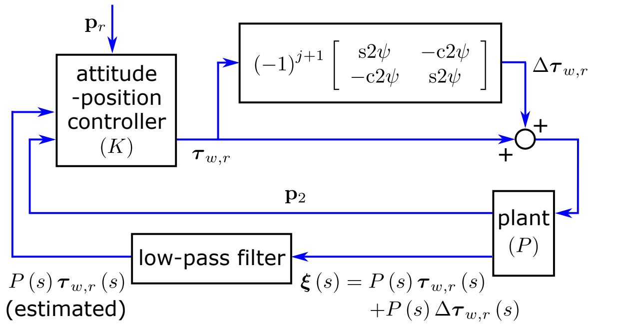

Fig. 4. A block diagram showing the principle of the closed-loop horizontal position control based on the reduced attitude dynamics. The implementation of the low-pass filter is specifically designed to remove the oscillatory leftover dynamics caused by the use of cyclic commands needed to deal with the severe underactuation of bicopters. Note that $s2\psi$ and $c2\psi$ are shorthands for $\sin(2\psi)$ and $\cos(2\psi)$.

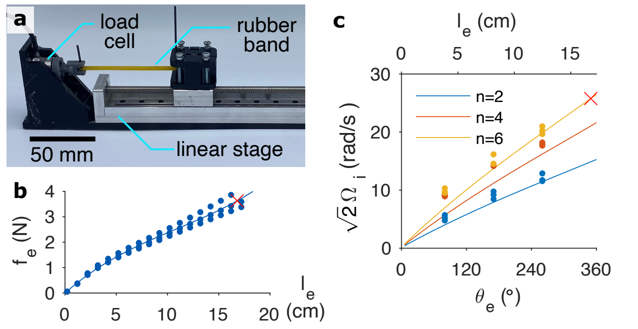

Fig. 5. (a) Photo of the experimental setup for the rubber band tensile test. (b) Force-deformation profile of the rubber bands. Empirical measurements are shown in dots and the line portrays the third-order polynomial fitted model. (c) Plot of the initial revolving rate of Bicopter-CCW ($\sqrt{2}\omega_i$) immediately after undocking obtained from the catapult-assisted take-off experiments. The measurements were taken with different amounts of preload by varying the number of elastic bands used (n) and the degree of elongation ($l_e = r_w\theta_e$). The dots represent measurements whereas model predictions are shown as lines. According to the energy-based model, ω_i is the predicted initial spinning rate for both bicopters in the mid-air disassembly.

$\Delta\boldsymbol{\tau}_{w,r}$ on the position control, a Chebyshev type II low-pass filter is employed to eliminate the effect of $\Delta\boldsymbol{\tau}_{w,r}$ on the measurements of $\boldsymbol{\xi}$ used in the computation of $\boldsymbol{\tau}_{w,r}$. The resultant closed-loop dynamics is illustrated by Fig. 4. Overall, the implementation of cyclic commands from (22) and the use of a low-pass filter to attenuate the leftover torque effectively enable the bicopters to be controllable in three degrees of freedom despite having only two independent actuators. The control performance of bicopters, however, would be affected in comparison with quadcopters.

V. Experimental Validation

Experiments are performed to evaluate the performance of the robots, including the undocking mechanism and bicopter flight performance. Finally, a mid-air transition of SplitFlyer Air from the quadcopter to bicopter mode is demonstrated.

A. Evaluation of Undocking Mechanism

In order to tune the amount of the preloaded energy for the catapult mechanism to obtain the desired spinning rate upon undocking, we performed tensile tests on rubber bands. The findings are subsequently incorporated into the models and further evaluated with the catapult-assisted take-off experiments. The force-deformation profile and the outcomes from the take-off experiments are to be used to realize the mid-air disassembly in the succeeding flight experiments.

1) Rubber band tensile test: We used a motorized linear stage for testing the tensile force of rubber bands. The platform allows the rubber bands to be stretched by up to 200 mm. A force sensor (ATI Nano17 Titanium) was affixed to the static side of the stage for measuring the tension generated by the rubber bands at different elongations as shown in Fig. 5a.

We conducted 18 steady-state measurements, at the interval of 10 mm, from 0 to 170 mm. The experiments were repeated with three different rubber bands of the same type to account for the minor variations between each rubber band, totaling 54 datapoints as reported in Fig. 5b. An empirical model was employed to capture the profile of f_e using the least squares fitting as shown in Fig. 5b. The third-order polynomial model produces the coefficient of determination of 0.98. Further increasing the order results in negligible improvement.

2) Characterization of elastic catapult mechanism: Based on the tensile test above, we carried out catapult-assisted take-off experiments to validate the launching speed of a bicopter as predicted by the energy-based model (2).

Instead of verifying the revolving speed of both bicopters from the mid-air split, for simplicity, we simulated the undocking process with Bicopter-CW (carrying the catapult base) fixed on the ground. Actuation of the SMA would then launch the Bicopter-CCW up with the initial yaw rate of $\sqrt{2}\omega_i = \sqrt{U(\theta_e)/I_z}$ as the elastic energy is transferred to only one bicopter. In the take-off experiments, we installed 2, 4, and 6 rubber bands on the undocking mechanism. In the loading step, three different loading angles ($\theta_e = 80°, 170°, 260°$) were investigated for each set of rubber bands. These corresponds to $l_e = r_w\theta_e = 3.8, 8.2, 12.5$ cm for $r_w = 2.75$ cm. The yaw rate of Bicopter-CCW immediately after the launch was extracted using the motion capture system (OptiTrack Prime 13w). With three trials performed for each setting, 27 datapoints of measured $\sqrt{2}\omega_i$ are plotted in Fig. 5c, alongside the model predictions from (2). The findings suggest that $\sqrt{2}\omega_i > 20$ rad·s^{-1} was achieved when six elastic bands were used.

From the results, it is observed that the model slightly under-predicts ω_i despite neglecting possible viscoelastic losses. This is possibly due to the nonuniform elongation of the bands and the fact that the actual stretch could be longer than $r_w\theta_e$ thanks to the band thickness and the overlaps from the winding. The root-mean-square error (RMSE) of the prediction of ω_i is 2.1 rad/s, one order of magnitude smaller than ω_i. This validates the energy-based model described by (2).

Based on these outcomes, six rubber bands and the preload angle of $\theta_e = 350°$ were chosen for the mid-air disassembly. The configuration, corresponding to red crosses in Fig. 5b and c, is conservatively anticipated to generate $\omega_i = 18.3$ rad·s^{-1} according to the model. This target ω_i is approximately one-third of ω_z^* as experimentally determined from flight experiments below. In Section V-C and the supplementary video, it is demonstrated that the catapult mechanism with selected arrangement facilitated the bicopters to reach their hovering states rapidly after undocking, enabling the mid-air disassembly to be achieved at low altitude.

B. Bicopter Flight Demonstration and Performance

Control performance of the developed flight controller is validated. Since the major novelty lies in the ability to control the position of bicopters, detailed evaluation with trajectory tracking is carried out in this section. The demonstration of flights in both quadcopter and bicopter modes together is provided in the mid-air disassembly tests in Section V-C.

1) Experimental setup: Flight experiments were carried out in a $3\times3\times2.5$-m^3 arena with six motion capture cameras (OptiTrack Prime 13w) for tracking the pose of the vehicles. The measurements were used for both flight control and ground-truth measurements. Flight controllers were implemented using Python on the ground station. From the received feedback, the ground station determined the robot's heading ψ, the inclination angles $\boldsymbol{\xi}$, and other quantities required to compute $\boldsymbol{\tau}_{w,r}$ and the total thrust at 200 Hz. These quantities were transmitted to the robots via radio communication (Bitcraze Carzyradio PA), through the use of Crazyflie Python API. The original flight controller is replaced with the custom code that maps the received instructions to the motor commands. The heading angle (yaw) was estimated onboard from integrating the angular rate (ω_z^*) from the motion capture system at 1 kHz and periodically corrected by the motion capture feedback. The onboard IMU was not used for control. Both control boards on the SplitFlyer Air functions independently and almost identically, controlling one pair of motors each in either flight mode. For Bicopter-CW, we employed a GPIO pin to trigger the installed SMA actuator through a separate motor driver (HR8833).

2) Trajectory tracking: To evaluate the flight performance of the bicopters, we designed two sets of trajectory tracking experiments: a smooth helical trajectory with a maximum flight speed of 1.26 ms^{-1} and a step trajectory.

To perform flights, Bicopter-CCW was first commanded to take off in open loop at extremely low altitude for ≈ 6 s. During this phase, the robot built up the necessary yaw rate while leveraging the ground effects for attitude stabilization. After reaching the equilibrium revolving speed, the robot tracked the prescribed trajectories for over 40 s before entering the landing phase. For each trajectory, five flight trials were conducted. For the step trajectory, the feedforward command (derivatives of $\mathbf{p}_r$) is absent during the location change. The plots of actualized trajectories and reference trajectories are shown in Fig. 6a and b (plots of ξ_x and ξ_y can be found in Fig. S3 and Fig. S4. The results reveal that the bicopter maintained the revolving rate of $\Omega_z^* \approx 55$ rad·s^{-1} when flying. This equates to almost 9 cycles per second. The fast yaw rate substantiates the cycle-averaged treatment through the neglect of zero-mean fast varying terms in the modeling and flight controller design.

We quantify the flight performance via the RMSEs from all five flights (from 5 to 50 s). For the helical trajectory, the RMSEs in the horizontal and vertical directions are 8.9 and 5.3 cm. For the step trajectory, the RMSEs in the horizontal and vertical directions are 25.0 cm and 2.5 cm. We believe that the observed errors are due to the combination of the linearization, inaccurate model coefficients and the underactuation of the robot. For the step trajectory, the absence of the feedforward input leads to the slow transient response. Video footage of an example helical trajectory tracking flight is provided as Supplementary Video.

The proposed controller benefits from the streamlined implementation. Despite the small-angle assumption, the flight performance is comparable to a nonlinear (no small angle-assumption but cascaded) implementation in [34]. To highlight the benefit obtained from the removal of the timescale separation assumption, we compare the proposed controller with the cascaded method in the previous study [25], the same tests were performed with the cascaded controller. Despite our best attempt in gain tuning, the robot was unable to complete the relatively fast helical trajectory and crashed within five seconds as seen in Fig. 6. For the step trajectory, the bicopter with the cascaded controller displayed pronounced oscillations around the reference trajectory. The resultant RMSEs in the horizontal and vertical directions (evaluated from 0 to 55 s) are 39.5 cm and 2.5 cm, considerably larger than that of the proposed controller. The outcomes show clear advantages and improvements in the control performance of the proposed controller, thanks to the simultaneous consideration of the attitude and translational dynamics.

All in all, the devised control law equips the severely underactuated bicopters with an ability to be placed anywhere in space, with the precision parallel to that of a regular multirotor robot.

C. Controlled SplitFlyer Air Flights with Mid-air Disassembly

To demonstrate and evaluate the ability to execute the flight mode transformation of SplitFlyer Air, we carried out the mid-air undocking experiments. In these experiments, SplitFlyer Air made a transition from the quadcopter configuration to bicopters, or split into two independent robots, mid-air.

To accomplish the transformation, the flight is divided into three stages: i) a take-off and flight in the quadcopter mode; ii) the transition; and iii) concurrent flights with two bicopters. Fig. 7 shows an image sequence illustrating the mid-flight disassembly, with the associated flight data given in Fig. 6c.

In the first phase, two bicopters were docked together as a quadcopter. The robot was controlled using the proposed strategy (Section IV-C1). The horizontal location of the robot was also controlled to ensure the flight stability in the tight space.

Once reaching the desired altitude, the quadcopter entered the second stage. The SMA actuator was activated, resulting in the release of elastic energy that impulsively assisted the bicopters to acquire sufficient initial revolving rates. This is to ensure that the bicopters rapidly stabilize and stay aloft in the restricted volume. According to Fig. 6c, the yaw rates of both bicopters were between 20-30 rad·s^{-1} immediately after the undocking process. Since the initial revolving rates

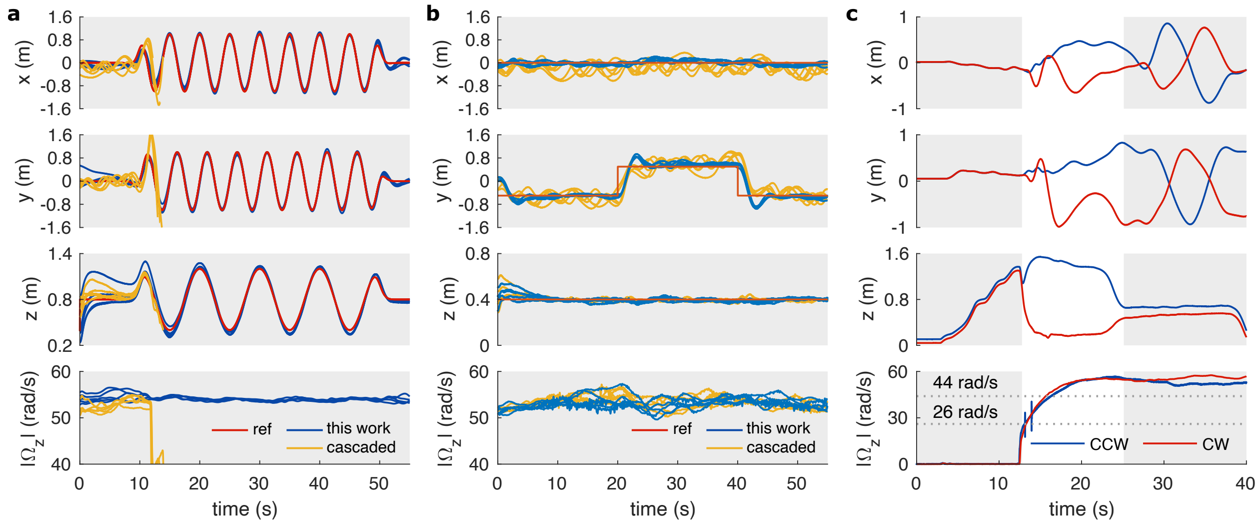

Fig. 6. (a) and (b) Flight data from the five repeated trajectory tracking experiments performed by Bicopter-CCW. (a) A 3D helical trajectory. Refer to Fig. S2 for closed-up plots with the effect of revolving motion visible. (b) A 1-m step trajectory with constant altitude. (c) An example flight trajectory of SplitFlyer Air prior to and after the disassembly into two bicopters.

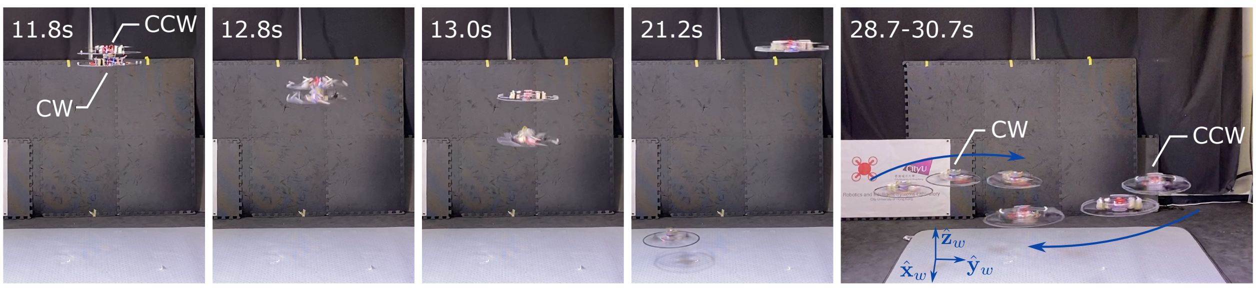

Fig. 7. A sequence of images that capture the quadcopter and its undocking process. The second and third frames highlight the SMA-actuated disassembly. The last composite image demonstrates two bicopters concurrently following their prescribed trajectories after the undocking.

were notably below the nominal $\omega_z^* \approx 53$ rad·s^{-1} and the bicopters' states deviated significantly from the assumed hovering conditions in the controller design, the robots would temporarily suffer from the deteriorated control performance.

To work around the difficulties associated with the undocking and transition process, the horizontal position control on each bicopter was briefly disabled during and instantly after the disassembly until the yaw rate rose to $|\omega_z| > 26$ rad·s^{-1}. In the meantime, the altitude setpoints for Bicopter-CCW and Bicopter-CW were prescribed to 1.5 m and 0.2 m to prevent an accidental collision. Between $26 < |\omega_z| < 44$ rad·s^{-1} (see Fig. 6c), we applied the horizontal position control method presented in [25] to loosely regulate the vehicles' positions. This is because the cascaded controller from [25] proves to be robust over a larger range of the revolving speed during flight experiments. However, without leveraging the feedback of $\dot{\boldsymbol{\xi}}$ for control, the cascaded method is visibly inferior to the proposed control laws when it comes to flight performance near the nominal hovering condition.

Once the bicopters acquired sufficient yaw rates or $|\omega_z| > 44$ rad·s^{-1}, the cascaded controller was replaced with the proposed controller. The robots spent ≈ 5 s in the transition phase with the reduced control effort. Despite that, both bicopters remained in the tight $2 \times 2 \times 1.6$ m volume. Subsequently, the bicopters slowly converged to their respective setpoints, marking the end of the transition. Both robots were then commanded to realize a circular trajectory as seen in Fig. 7 and the supplementary video. Four additional SplitFlyer Air flights with mid-air disassembly were performed. The vehicle illustrated trajectories with highly similar characteristics, verifying the reliability of the undocking mechanism and the proposed control strategy. The footage of these transitional flights can be found in the supplementary video.

VI. Conclusion

In this work, we have developed a transformable multirotor robot–SplitFlyer Air. In addition to the quadcopter mode, SplitFlyer Air separates into two flight-capable bicopters that can function independently. The two modes of aerial locomotion are vastly different. In the bicopter configuration, the robots, possessing only two actuators, are severely underactuated. Yet, thanks to the proposed flight control methods, the vehicles demonstrate stable flights in both regimes. Furthermore, the autonomous transition from the quadcopter form to bicopters through assistance from the developed undocking mechanism is achieved. All in all, SplitFlyer Air is an aerial platform with the potential for swarms with scalability.

REFERENCES

[1] D. Floreano and R. J. Wood, "Science, technology and the future of small autonomous drones," *Nature*, vol. 521, no. 7553, pp. 460–466, 2015.

[2] A. Kalantari and M. Spenko, "Modeling and performance assessment of the hytaq, a hybrid terrestrial/aerial quadrotor," *IEEE Transactions on Robotics*, vol. 30, no. 5, pp. 1278–1285, 2014.

[3] Q. Tan, X. Zhang, H. A. F. T. Liu, S. Jiao, M. Zhou, and J. Li, "Multimodal dynamics analysis and control for amphibious fly-drive vehicle," *IEEE/ASME Transactions on Mechatronics*, 2021.

[4] Y. H. Tan and B. M. Chen, "Thruster allocation and mapping of aerial and aquatic modes for a morphable multimodal quadrotor," *IEEE/ASME Transactions on Mechatronics*, vol. 25, no. 4, pp. 2065–2074, 2020.

[5] K. McGuire, C. De Wagter, K. Tuyls, H. Kappen, and G. de Croon, "Minimal navigation solution for a swarm of tiny flying robots to explore an unknown environment," *Science Robotics*, vol. 4, no. 35, p. eaaw9710, 2019.

[6] S.-J. Chung, A. A. Paranjape, P. Dames, S. Shen, and V. Kumar, "A survey on aerial swarm robotics," *IEEE Transactions on Robotics*, vol. 34, no. 4, pp. 837–855, 2018.

[7] K. Mohammadi, S. Sirouspour, and A. Grivani, "Control of multiple quad-copters with a cable-suspended payload subject to disturbances," *IEEE/ASME Transactions on Mechatronics*, vol. 25, no. 4, pp. 1709–1718, 2020.

[8] S. Tan, S. Zhong, and P. Chirarattananon, "A one-step visual-inertial ego-motion estimation using photometric feedback," *IEEE/ASME Transactions on Mechatronics*, pp. 1–1, 2021.

[9] S. Zhong and P. Chirarattananon, "An efficient iterated ekf-based direct visual-inertial odometry for mavs using a single plane primitive," *IEEE Robotics and Automation Letters*, vol. 6, no. 2, pp. 486–493, 2021.

[10] D. Saldana, B. Gabrich, G. Li, M. Yim, and V. Kumar, "Modquad: The flying modular structure that self-assembles in midair," in *2018 IEEE International Conference on Robotics and Automation (ICRA)*. IEEE, 2018, pp. 691–698.

[11] T. Anzai, M. Zhao, M. Murooka, F. Shi, K. Okada, and M. Inaba, "Design, modeling and control of fully actuated 2d transformable aerial robot with 1 dof thrust vectorable link module," in *2019 IEEE/RSJ International Conference on Intelligent Robots and Systems (IROS)*. IEEE, 2019, pp. 2820–2826.

[12] B. Mu and P. Chirarattananon, "Universal flying objects: Modular multirotor system for flight of rigid objects," *IEEE Transactions on Robotics*, vol. 36, no. 2, pp. 458–471, 2020.

[13] N. Zhao, W. Yang, C. Peng, G. Wang, and Y. Shen, "Comparative validation study on bioinspired morphology-adaptation flight performance of a morphing quad-rotor," *IEEE Robotics and Automation Letters*, vol. 6, no. 3, pp. 5145–5152, 2021.

[14] D. Saldana, P. M. Gupta, and V. Kumar, "Design and control of aerial modules for inflight self-disassembly," *IEEE Robotics and Automation Letters*, vol. 4, no. 4, pp. 3410–3417, 2019.

[15] R. Oung and R. D'Andrea, "The distributed flight array: Design, implementation, and analysis of a modular vertical take-off and landing vehicle," *The International Journal of Robotics Research*, vol. 33, no. 3, pp. 375–400, 2014.

[16] M. Zhao, T. Anzai, F. Shi, X. Chen, K. Okada, and M. Inaba, "Design, modeling, and control of an aerial robot dragon: A dual-rotor-embedded multilink robot with the ability of multi-degree-of-freedom aerial transformation," *IEEE Robotics and Automation Letters*, vol. 3, no. 2, pp. 1176–1183, 2018.

[17] E. R. Ulrich, J. S. Humbert, and D. J. Pines, "Pitch and heave control of robotic samara micro air vehicles," *Journal of Aircraft*, vol. 47, no. 4, pp. 1290–1299, 2010.

[18] S. Bai and P. Chirarattananon, "Design and take-off flight of a samara-inspired revolving-wing robot," in *2019 IEEE/RSJ International Conference on Intelligent Robots and Systems (IROS)*. IEEE, 2019, pp. 6070–6076.

[19] P. Chirarattananon, K. Y. Ma, and R. J. Wood, "Perching with a robotic insect using adaptive tracking control and iterative learning control," *The International Journal of Robotics Research*, vol. 35, no. 10, pp. 1185–1206, 2016.

[20] Z. Tu, F. Fei, and X. Deng, "Untethered flight of an at-scale dual-motor hummingbird robot with bio-inspired decoupled wings," *IEEE Robotics and Automation Letters*, vol. 5, no. 3, pp. 4194–4201, 2020.

[21] W. Zhang, M. W. Mueller, and R. D'Andrea, "Design, modeling and control of a flying vehicle with a single moving part that can be positioned anywhere in space," *Mechatronics*, vol. 61, pp. 117–130, 2019.

[22] A. Lanzon, A. Freddi, and S. Longhi, "Flight control of a quadrotor vehicle subsequent to a rotor failure," *Journal of Guidance, Control, and Dynamics*, vol. 37, no. 2, pp. 580–591, 2014.

[23] M. W. Mueller and R. D'Andrea, "Relaxed hover solutions for multicopters: Application to algorithmic redundancy and novel vehicles," *The International Journal of Robotics Research*, vol. 35, no. 8, pp. 873–889, 2016.

[24] S. Sun, L. Sijbers, X. Wang, and C. de Visser, "High-speed flight of quadrotor despite loss of single rotor," *IEEE Robotics and Automation Letters*, vol. 3, no. 4, pp. 3201–3207, 2018.

[25] S. Bai, S. Tan, and P. Chirarattananon, "Splitflyer: a modular quadcoptor that disassembles into two flying robots," in *2020 IEEE/RSJ International Conference on Intelligent Robots and Systems (IROS)*. IEEE, 2020, pp. 1207–1214.

[26] D. Mellinger, N. Michael, and V. Kumar, "Trajectory generation and control for precise aggressive maneuvers with quadrotors," *The International Journal of Robotics Research*, vol. 31, no. 5, pp. 664–674, 2012.

[27] M. Bangura and R. Mahony, "Thrust control for multirotor aerial vehicles," *IEEE Transactions on Robotics*, vol. 33, no. 2, pp. 390–405, 2017.

[28] M. Faessler, A. Franchi, and D. Scaramuzza, "Differential flatness of quadrotor dynamics subject to rotor drag for accurate tracking of high-speed trajectories," *IEEE Robotics and Automation Letters*, vol. 3, no. 2, pp. 620–626, 2017.

[29] S. Jameson, B. Satterfield, C. Bolden, H. Youngren, and N. Allen, "Samarai nano air vehicle–a revolution in flight," in *AUVSI Unmanned Systems North America Conference Proceedings*, 2007.

[30] H. Youngren, S. Jameson, and B. Satterfield, "Design of the samarai monowing rotorcraft nano air vehicle," in *Proceedings of the American Helicopter Society AHS 65th Annual Forum and Technology Display*, 2009.

[31] D. Vivet, P. Checchin, and R. Chapuis, "Line-based slam with slow rotating range sensors: results and evaluations," in *2010 11th International Conference on Control Automation Robotics & Vision*. IEEE, 2010, pp. 423–430.

[32] K. P. Jain and M. W. Mueller, "Flying batteries: In-flight battery switching to increase multirotor flight time," in *2020 IEEE International Conference on Robotics and Automation (ICRA)*. IEEE, 2020, pp. 3510–3516.

[33] R. Gill and R. D'Andrea, "Propeller thrust and drag in forward flight," in *2017 IEEE Conference on Control Technology and Applications (CCTA)*. IEEE, 2017, pp. 73–79.

[34] S. Sun, X. Wang, Q. Chu, and C. d. Visser, "Incremental nonlinear fault-tolerant control of a quadrotor with complete loss of two opposing rotors," *IEEE Transactions on Robotics*, vol. 37, no. 1, pp. 116–130, 2021.

[35] S. Crandall, "The effect of damping on the stability of gyroscopic pendulums," *ZAMP. Zeitschrift fÃŒr angewandte Mathematik und Physik*, vol. 46, 01 1995.

[36] Y. Chen, H. Zhao, J. Mao, P. Chirarattananon, E. F. Helbling, N.-s. P. Hyun, D. R. Clarke, and R. J. Wood, "Controlled flight of a microrobot powered by soft artificial muscles," *Nature*, vol. 575, no. 7782, pp. 324–329, 2019.

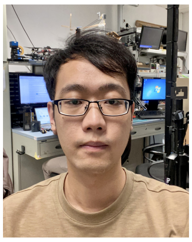

Songnan Bai received the B.S. degree in mechanical engineering from Xi'an Jiaotong University, Xi'an, China, in 2017, and the M.Sc. in Mechanical Engineering from City University of Hong Kong, Hong Kong SAR. He is currently pursuing the PhD degree with the Department of Biomedical Engineering, City University of Hong Kong.

Pakpong Chirarattananon (S'12-M'15) received the B.A. degree in Natural Sciences from the University of Cambridge, U.K., in 2009, and the Ph.D. degree in Engineering Sciences from Harvard University, Cambridge, MA, USA, in 2014.

He is currently an Associate Professor with the Department of Biomedical Engineering, City University of Hong Kong, Hong Kong SAR. His research interests include bio-inspired robots, micro air vehicles, and the applications of control and dynamics in robotic systems.

Supplementary materials for

SplitFlyer Air: A Modular Quadcopter that Disassembles into Two Bicopters Mid-Air

Songnan Bai and Pakpong Chirarattananon

S1. State-Space Representation of Dynamics and Controller

The flight dynamics can be expressed by a state-space representation. Based on the reduced attitude dynamics (14) and near-hovering translational dynamics (12), the system described by (12) and (14) is linear and fourth-order. Since $\ddot{\mathbf{p}} = g\mathbf{J}\xi$, we may define a state vector

$$\begin{aligned}\mathbf{x} &= \left[\begin{array}{cccc} \mathbf{p}_2^{\mathrm{T}} & \dot{\mathbf{p}}_2^{\mathrm{T}} & \boldsymbol{\xi}^{\mathrm{T}} & \dot{\boldsymbol{\xi}}^{\mathrm{T}} \end{array}\right]^{\mathrm{T}} \\ &= \left[\begin{array}{cccccccc} x & y & \dot{x} & \dot{y} & \xi_x & \xi_y & \dot{\xi}_x & \dot{\xi}_y \end{array}\right]^{\mathrm{T}},\end{aligned} \tag{S1}$$

such that the dynamics follow

$$\dot{\mathbf{x}} = \mathbf{A}_{ss}\mathbf{x} + \mathbf{B}_{ss}\mathbf{u}, \tag{S2}$$

where

$$\mathbf{A}_{ss} = \left[\begin{array}{cccc} \mathbf{0} & \mathbf{1} & \mathbf{0} & \mathbf{0} \\ \mathbf{0} & \mathbf{0} & g\mathbf{J} & \mathbf{0} \\ \mathbf{0} & \mathbf{0} & \mathbf{0} & \mathbf{1} \\ \mathbf{0} & \mathbf{0} & \mathbf{0} & -D_\xi\mathbf{1} - I_z\Omega_z^*\mathbf{J} \end{array}\right], \tag{S3}$$

$$\mathbf{B}_{ss} = \left[\begin{array}{cccc} \mathbf{0} & \mathbf{0} & \mathbf{0} & \mathbf{1} \end{array}\right]^{\mathrm{T}}, \tag{S4}$$

and the input

$$\mathbf{u} = \boldsymbol{\tau}_w, \tag{S5}$$

with $\mathbf{1}$ being a 2×2 identity matrix, $\mathbf{0}$ being a 2×2 zero matrix. As mentioned in Section III-D2, the yaw angle is not considered in this step.

With the assumption that the bicopter or quadcopter is able to arbitrarily generate torque about its $\hat{\mathbf{x}}_b$ and $\hat{\mathbf{y}}_b$ axes at any instance, the proposed control law in Section IV-B is obtained by solving (19), this results in

$$\mathbf{u} = -\mathbf{K}_1\left(\mathbf{x} - \mathbf{x}_r\right) + \mathbf{K}_2\mathbf{x} - \frac{I_d}{g}\mathbf{J}\mathbf{p}_r^{(4)}, \tag{S6}$$

with

$$\mathbf{K}_1 = -\left[\begin{array}{cccc} \frac{\lambda_0 I_d}{g}\mathbf{J} & \frac{\lambda_1 I_d}{g}\mathbf{J} & \lambda_2 I_d\mathbf{1} & \lambda_3 I_d\mathbf{1} \end{array}\right] \tag{S7}$$

$$\mathbf{K}_2 = \left[\begin{array}{cccc} 0 & 0 & 0 & D_\xi\mathbf{1} + I_z\omega_z^*\mathbf{J} \end{array}\right]. \tag{S8}$$

The first term term in (S6), containing the mismatch between the current and reference trajectories, is responsible for correction. The second term is for feedback linearization, cancelling out the left over dynamics corresponding to the last element in $\mathbf{A}_{ss}$. The last term in (S6) is the feedforward command depending on the predefined trajectory.To illustrate the architecture of the control system, we define a "plant" as the transfer function that maps $\mathbf{u}(s)$ to $\mathbf{x}(s)$, the block diagram of the close-loop system is presented in Fig. S1. Therein, the state and input of the system are presented in the Laplace domain.

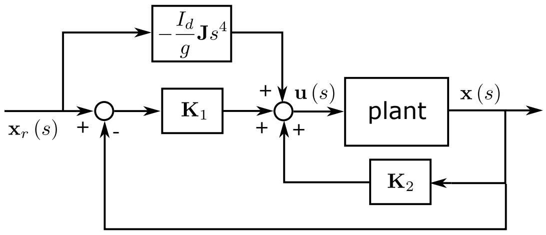

Fig. S1. Block diagram of the control architecture of the bicopor/quadcopter.

Supplementary Figures

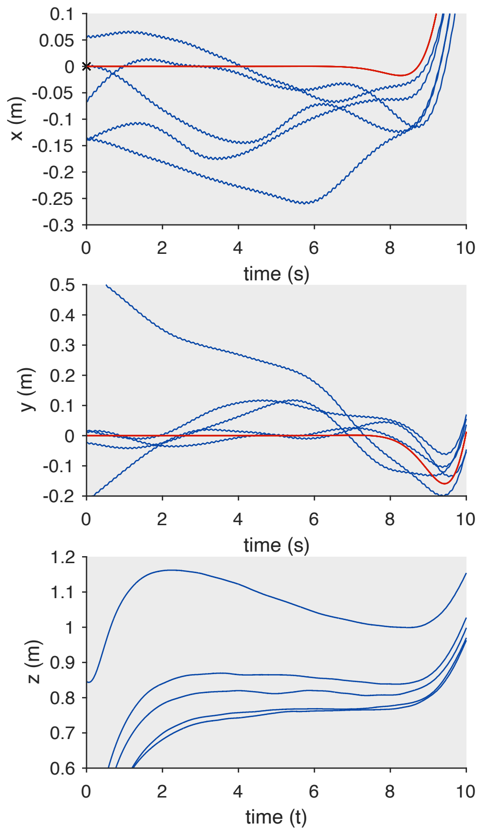

Fig. S2. The close-up view of Fig. 6a for t =0-10 s. The amplitude of the oscillation due to the rotating motion is less than 1 cm.

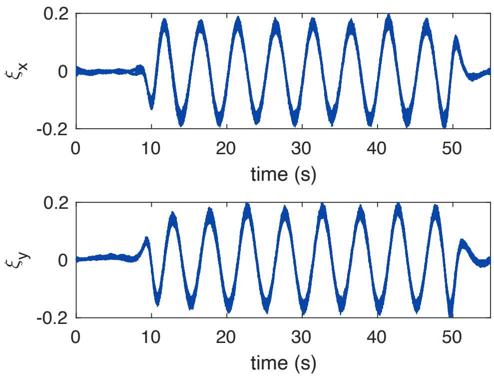

Fig. S3. The robot instantaneous attitude represented by ξ_x and ξ_y from the helical trajectory tracking flight. The figure includes ξ_x and ξ_y from five flights.

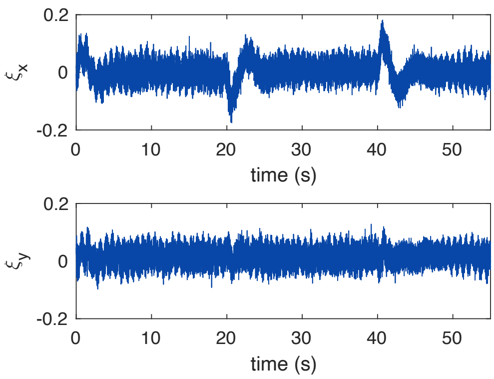

Fig. S4. The robot instantaneous attitude represented by ξ_x and ξ_y in step trajectory tracking flight. The figures include ξ_x and ξ_y in five flights.